Nanoscale

ROYAL SOCIETY OF CHEMISTRY

PAPER

View Article Online
View Journal | View Issue

Check for updates

Cite this: *Nanoscale*, 2026, **18**, 9689

Metastable cubic Cu_3SbS_3: a facile solution-phase access to a kinetic polymorph

Rittika Dhar,[a] Anil Kumar B. M.,[a] Pranav Negi,[b] Shuva Biswas,[c] Dirtha Sanyal[d,e] and Satya N. Guin*[a]

Received 6th January 2026,
Accepted 6th April 2026

DOI: 10.1039/d6nr00071a

rsc.li/nanoscale

Polymorphism in inorganic solids is central to controlling their structure–property relationships, yet stabilising high-energy phases remains challenging. Cu_3SbS_3, a ternary copper chalcogenide, exhibits rich structural diversity, but its metastable cubic polymorph (space group $I\bar{4}3m$) has thus far eluded stabilisation in pristine form. Here we report the room-temperature stabilisation of cubic Cu_3SbS_3 nanocrystals *via* a simple low-temperature solution-phase synthesis. Structural and spectroscopic analysis confirm the formation of phase-pure cubic nanocrystals with a band gap of ~1.86 eV. Thermal studies, including high-temperature powder X-ray diffraction and positron annihilation spectroscopy, reveal that the cubic phase is kinetically stabilised up to ~623 K, beyond which it undergoes an irreversible transformation into orthorhombic and tetrahedrite-type phases, assisted by Sb and S-vacancy formation. The metastable cubic Cu_3SbS_3 nanocrystals exhibit p-type semiconducting behaviour and ultralow thermal conductivity (~0.77 W m^{-1} K^{-1} at 303 K). The low thermal transport originates from strong anharmonicity induced by stereochemically active Sb $5s^2$ lone pairs and local Cu coordination distortions. These findings demonstrate that nanoscale synthesis enables access to otherwise inaccessible metastable polymorphs and uncover the thermally driven pathways governing their structural evolution. This study extends the accessible phase space of chalcogenides, offering new possibilities for tailoring their optoelectronic and thermoelectric properties.

Introduction

The synthesis of inorganic materials with diverse crystal structures is important for both fundamental understanding and technological applications. A key concept in solid-state chemistry is polymorphism,[1–5] wherein a single compound can adopt multiple crystal structures despite having the same chemical composition. Since crystal structure strongly influences electronic, optical, magnetic, and thermal properties, access to different polymorphs is essential for understanding and tailoring material functionality. The stability of a given polymorph is determined by its relative Gibbs free energy under specific thermodynamic conditions. Generally, thermodynamically stable polymorphs are synthesised *via* high-temperature solid-state reactions,[6–8] whereas metastable or kinetically trapped phases are often difficult to access by such routes.[1,6–9] These kinetically stable or metastable phases, although not the lowest in energy, are of considerable interest for exploring novel structural, chemical, and physicochemical properties. The synthesis and stabilisation of metastable phases provide important insights into energy landscapes and structural frameworks fundamental to advanced material design.

Nanocrystals offer a particularly attractive route for accessing such unconventional crystal structures and precisely tailored material properties. In nano-dimension, the increased surface-to-volume ratio leads to elevated surface energy and lower lattice energy compared to their bulk counterpart. These features lower the activation energy required for structural transformations, thereby facilitating solid–solid phase transitions and stabilisation of certain structures that may be hindered in bulk analogues.[10–12] Various wet-chemical methods have been developed for the synthesis of nanomaterials, including seeded growth,[13] polyol synthesis,[14] solvothermal processes,[15] and hot-injection techniques.[16] In low-temperature solution-based synthesis, phase formation is predominantly governed by kinetic,[17] rather than thermodynamic control. This often facilitates the stabilisation of higher-energy

---

[a] Department of Chemistry, Birla Institute of Technology and Science Pilani, Hyderabad Campus, Jawahar Nagar, Hyderabad 500078, India. E-mail: satyanarayan.g@hyderabad.bits-pilani.ac.in
[b] Department of Chemistry, Indian Institute of Science Education and Research Bhopal, Bhopal 462 066, India
[c] New Chemistry Unit, Jawaharlal Nehru Centre for Advanced Scientific Research (JNCASR), Jakkur P.O., Bengaluru 560064, India
[d] Variable Energy Cyclotron Centre, 1/AF Bidhannagar, Kolkata 700064, India
[e] Homi Bhabha National Institute, Training School Complex, Anushakti Nagar, Mumbai 400094, India

metastable phases under ambient conditions, which are typically difficult to access *via* conventional high-temperature routes. Several metastable nanocrystalline polymorphs have been realised through such routes, including $Ge_2Sb_2Te_5$,[18] $Pb_mSb_{2n}Te_{m+3n}$ homologous series,[19] $CuInSe_2$,[20] Cu_2SnSe_3,[21] Cu_2ZnSnS_4,[22,23] tetragonal β-Ag_2Se,[24] orthorhombic MnAs,[25] $Pb_{2-x}Sn_xS_2$,[26] and wurtzite-type γ-MnSe,[27] $Cu_2BaSnS_{4-x}Se_x$ [28] Cu_2Te.[29] These examples highlight the importance of nanoscale synthesis in expanding the accessible phase space of functional inorganic materials.

Copper and silver-based chalcogenide compounds have emerged as materials of significant interest owing to their applicability in thermoelectric energy conversion and photovoltaics. Recently, particular attention has been devoted to ternary systems including Cu–Sb–Se and Cu–Sb–S,[30–35] which offer a unique combination of non-toxicity, elemental abundance, and promising electronic and thermal transport properties. Among these, the Cu_3SbSe_3, Cu_3SbSe_4 and Cu_3SbS_4 phases have been shown promise for thermoelectric applications due to their intrinsically low lattice thermal conductivity.[36–38] The presence of stereochemically active $5s^2$ lone-pair electrons on Sb atoms, which induce pronounced bond anharmonicity and soft phonon modes, leads to such low thermal transport behaviour.[36,39]

Cu_3SbS_3 is an intriguing member of the Cu–Sb–S ternary chalcogenide family, notable for its rich polymorphism and pronounced structural phase transitions upon thermal treatment.[40–42] At temperatures below 263 K, Cu_3SbS_3 crystallises in an orthorhombic lattice with the $P2_12_12_1$ space group. Between 263 K and 395 K, it adopts a monoclinic structure (space group $P2_1/c$). Upon further heating above 395 K, a second phase transition occurs, leading to an orthorhombic structure with the *Pnma* space group (Fig. S1). Additionally, the existence of a high-energy metastable cubic phase adopting the tetrahedrite structure ($I\bar{4}3m$ space group) is also discussed in the literature (Fig. 1a).[43] In the cubic phase, half of the Cu atoms reside in distorted four-coordinated tetrahedral sites [CuS_4], while the remaining half occupy three-coordinated triangular sites [CuS_3]. The absence of one sulfur atom (denoted as ◊) in the [CuS_3] unit removes a vertex from the triangle, yielding an open isosceles configuration denoted as [CuS_2◊]. Such configurations lead to additional degrees of freedom for Cu atom, which induces rattling vibrations (Fig. 1b).[44] The Sb atoms are positioned in tetrahedral sites but bond to only

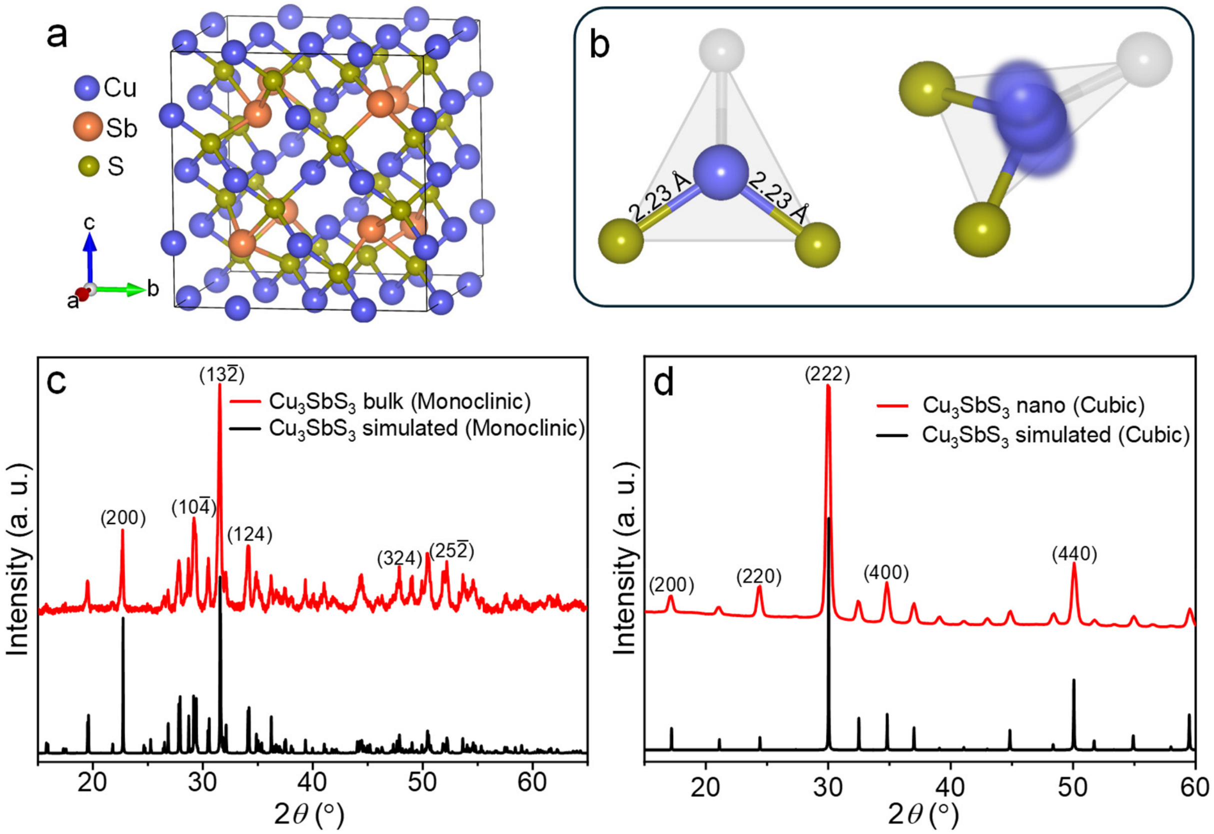

Fig. 1 (a) Crystal structure of Cu_3SbS_3 adopting a cubic structure ($I\bar{4}3m$ space group). (b) Left panel: the isosceles [CuS_2◊] unit formed by a vertex-deficient [CuS_3] triangle. Right panel: the associated vibrational freedom of the Cu atom, enabled by the open coordination. (c) Room temperature PXRD pattern of monoclinic (space group $P2_1/c$) bulk Cu_3SbS_3 with the simulated pattern (COD: 00-900-4360). (d) Room temperature PXRD pattern of as-synthesised cubic (space group $I\bar{4}3m$) nanocrystalline Cu_3SbS_3 with the simulated pattern (COD: 00-101-0508).

three sulfur atoms, forming distinctive SbS_3 pyramids. This coordination leaves the Sb 5s lone pair electrons oriented toward the unoccupied vertex of the tetrahedron. The presence of active lone pairs and rattling vibrations in cubic-Cu_3SbS_3 makes it a promising candidate for intrinsic low thermal conductivity. Yet, stabilisation of cubic-Cu_3SbS_3 remains challenging in its pristine form. Conventionally, stabilisation has been achieved through substitution of transition metals (Fe, Co, Ni) at the Sb site, which intrun reduces structural dimensionality.[39,45] The influence of reduced dimensionality on crystal symmetry suggests that low-temperature, solution-based methods could offer a promising approach for stabilising metastable Cu_3SbS_3 polymorph in its pristine form. However, in most cases, these methods tend to yield a low-energy monoclinic phase,[45] and reports of stabilised cubic Cu_3SbS_3 remain scarce in the literature.

In this study, we report the successful stabilisation of the metastable cubic phase of Cu_3SbS_3 at room temperature in nanocrystalline form using a simple low-temperature solution-based synthesis approach. The nanocrystals have been characterised using powder X-ray diffraction (PXRD), X-ray photoelectron spectroscopy (XPS), field emission scanning electron microscopy (FESEM), and transmission electron microscopy (TEM). Room temperature PXRD pattern confirms the stabilisation of metastable cubic Cu_3SbS_3 phase in the $I\bar{4}3m$ space group. Differential Scanning Calorimetry (DSC) measurements reveal that kinetically stabilised cubic nanocrystals exhibit temperature-driven unusual phase transformation. To understand such thermally induced phase transformation behaviour and structural information, we have performed a temperature-dependent PXRD study and positron annihilation spectroscopy. Analysis of DSC and temperature-dependent heating–cooling PXRD data reveals that the metastable cubic phase remains stable up to ~623 K. Upon further heating and subsequent cooling, it irreversibly transforms into a mixture of cubic tetrahedrite and orthorhombic Cu_3SbS_3 phases. Positron annihilation spectroscopy measurements show the formation of a large number of Sb and S vacancies at higher temperatures, which facilitates phase separation. The kinetically trapped metastable phase transitions into thermodynamically stable structures upon thermal treatment and does not revert back to the original cubic phase during cooling.

Results and discussion

Nanocrystalline cubic-phase of Cu_3SbS_3 was synthesised *via* a facile solution-based approach employing ethanolamine as both solvent and coordinating agent. Copper nitrate trihydrate and antimony acetate served as the respective copper and antimony precursors, while elemental sulfur was used as an anionic source in the ethanolamine medium. The reaction mixture was subsequently heated to 150 °C for 30 minutes and then allowed to cool naturally to ambient temperature. This low-temperature, solution-mediated process, coupled with nanoscale particle formation, effectively stabilises the kinetically favoured cubic phase of Cu_3SbS_3 at room temperature. Phase purity and composition were conclusively established through powder X-ray diffraction (PXRD), X-ray photoelectron spectroscopy (XPS), Field emission scanning electron microscopy (FE-SEM), transmission electron microscopy (TEM), energy-dispersive X-ray spectroscopy (EDX), and selected area electron diffraction (SAED) analysis. For comparison, bulk synthesis was conducted by using stoichiometric amounts of elemental copper (Cu), antimony (Sb), and sulfur (S) in vacuum-sealed quartz ampoules. The ampoule was subjected to a controlled heating protocol, slowly ramping the temperature to 900 °C over a period of 12 hours, and soaked at this temperature for 48 hours before quenching in ice-cold water.

In Fig. 1c and d, we present the room-temperature powder X-ray diffraction (XRD) patterns for both bulk and nanocrystalline Cu_3SbS_3 samples alongside their respective simulated patterns. The bulk Cu_3SbS_3 synthesised using the conventional high-temperature solid-state method shows the PXRD patterns corresponding to the monoclinic phase (space group $P2_1/c$) (Fig. 1c). Thus, attempts to stabilise the metastable cubic phase in bulk samples by rapid quenching in ice-cold water were unsuccessful. The experimental PXRD pattern of the nanocrystalline sample synthesised *via* the low-temperature solution-phase route exhibits excellent agreement with the simulated pattern corresponding to the cubic phase (space group $I\bar{4}3m$) (Fig. 1d and Fig. S5), which is further supported by the Rietveld refinement (Fig. S2 and Table S1). Therefore, the PXRD analysis of both bulk and nanocrystals indicates that pristine cubic Cu_3SbS_3 cannot be accessed *via* high-temperature, thermodynamically controlled routes. The observations also reveal that the metastable pristine cubic phase of Cu_3SbS_3

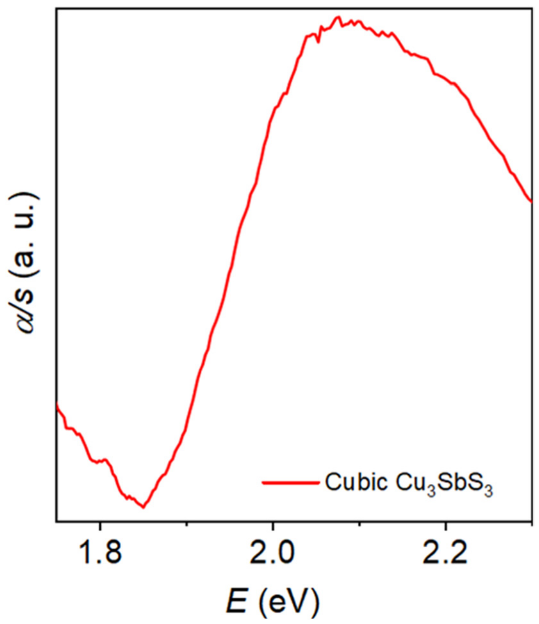

Fig. 2 Optical absorption spectra of cubic nanocrystalline Cu_3SbS_3 measured at room temperature.

can only be stabilised through nanoscale synthesis under low-temperature conditions, highlighting the importance of the synthetic route on phase selectivity. The as-synthesised nanocrystalline cubic Cu_3SbS_3 is a semiconductor in nature, as evident from optical band gap measurements. The spectroscopically measured optical band gap of cubic Cu_3SbS_3 nanocrystal is ~1.86 eV (Fig. 2), which is significantly blue-shifted relative to the as-synthesised bulk monoclinic counterpart (~1.65 eV) (Fig. S9).

The field-emission scanning electron microscopy (FESEM) images reveal that the Cu_3SbS_3 nanocrystals are nearly monodisperse, exhibiting nearly uniform size and morphology throughout the sample (Fig. 3a and b). Energy-dispersive X-ray (EDX) analysis confirms that the actual elemental composition is $Cu_{3.15}SbS_{3.04}$, which is in close agreement with nominal composition (Fig. S3). Furthermore, elemental mapping demonstrates a homogeneous distribution of Cu, Sb, and S within the nanocrystals, affirming the single-phase nature and compositional uniformity of the synthesised material (Fig. 3c–f). To further understand the morphology and microstructure, transmission electron microscopy (TEM) and electron diffraction analysis were performed at room temperature for the synthesised nanocrystals (Fig. 4). The particle size distribution histogram derived from TEM images reveals a diameter ranging from 45 to 55 nm, with an average of ~51.33 nm (Fig. S4). This is reasonably consistent with the crystallite size (~34.95 nm) estimated from XRD peak broadening using Scherrer analysis, considering the difference between particle and crystallite size (Table S2). Furthermore, the selected area electron diffraction (SAED) pattern obtained from a single par-

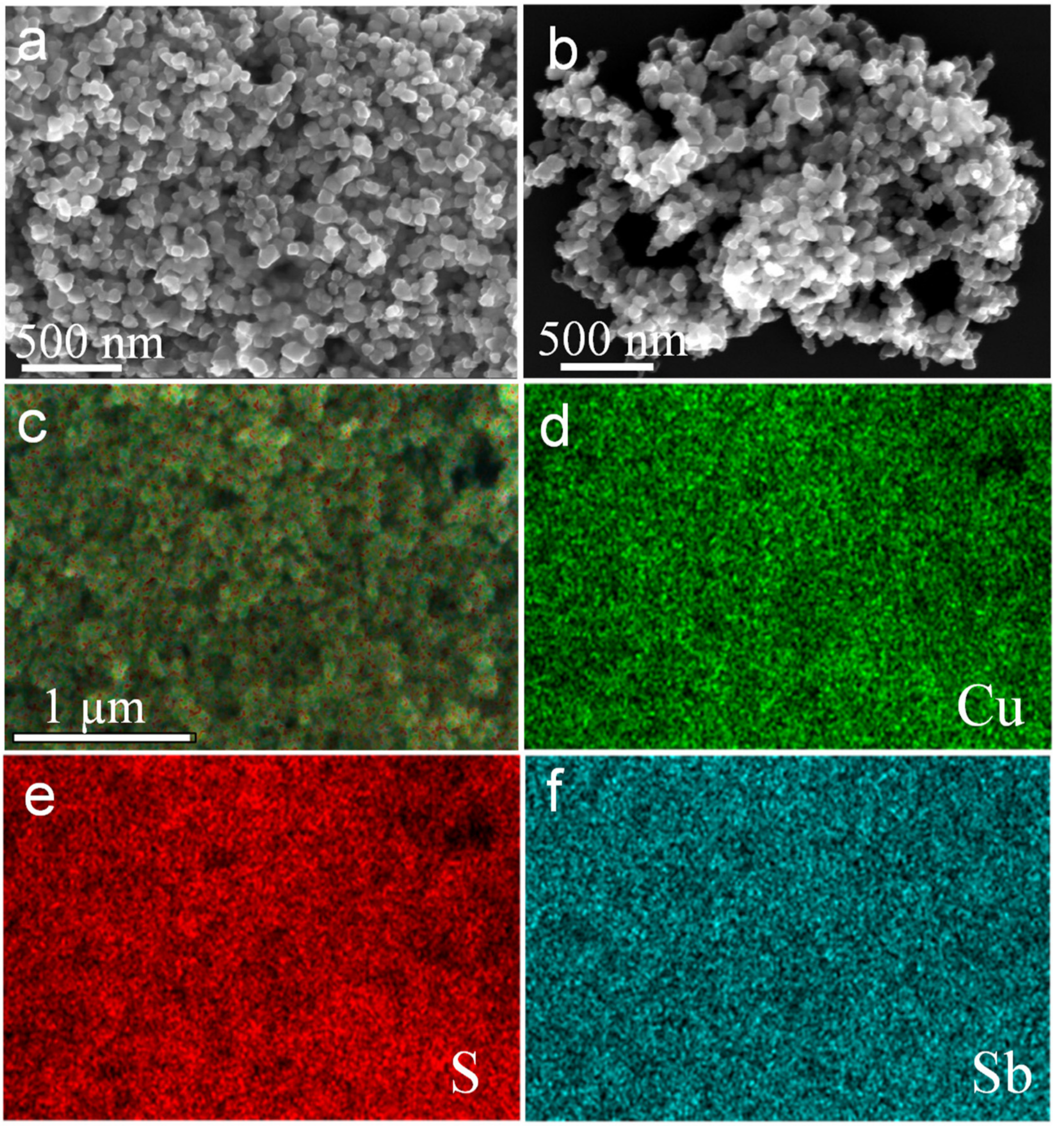

Fig. 3 (a) and (b) Field emission scanning electron microscopy (FESEM) images of Cu_3SbS_3 nanocrystals. (c)–(f) Energy-dispersive X-ray spectroscopy (EDX) elemental mapping of Cu_3SbS_3 nanocrystals. The mapping confirms the homogeneous distribution of constituent elements Cu, Sb and S.

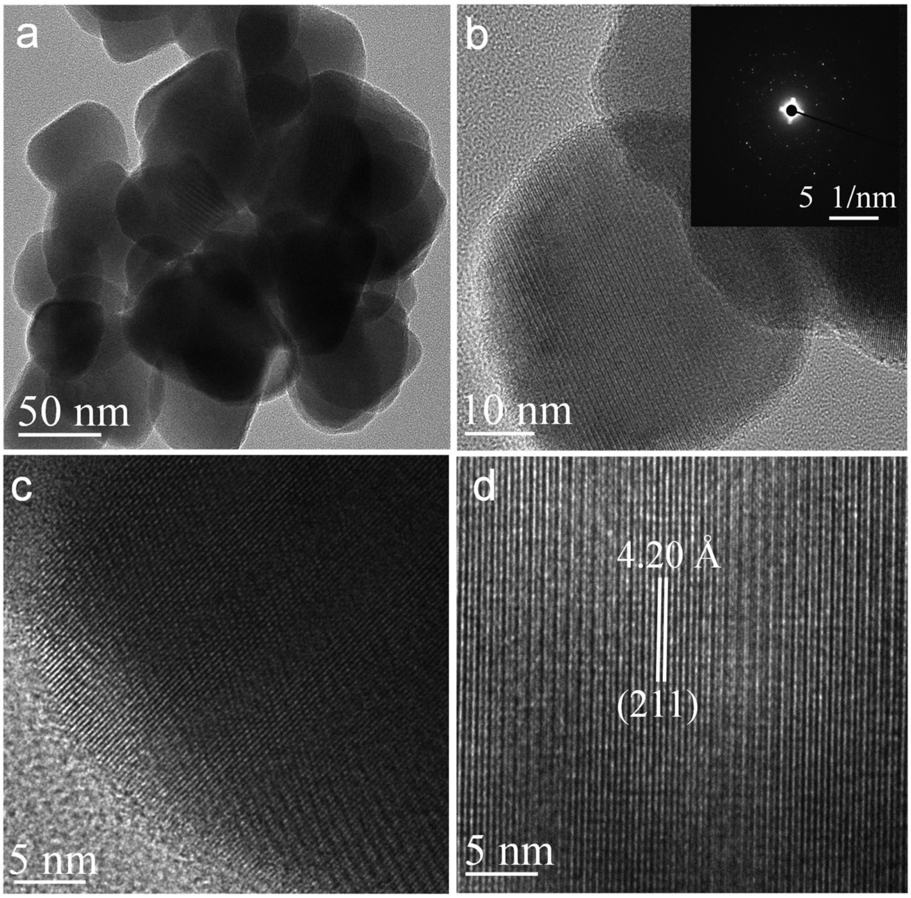

Fig. 4 (a) and (b) Transmission electron microscopy (TEM) images of Cu3SbS3 nanocrystals; the inset (b) shows the corresponding SAED pattern, (c) and (d) high-resolution-TEM (HRTEM) images showing (211) lattice planes.

ticle (inset of Fig. 4b) indicates the crystalline nature of the nanoparticle. High-resolution TEM (HRTEM) images display well-defined lattice fringes with an interplanar spacing of 4.20 Å, which can be indexed to the (211) crystallographic plane of cubic Cu_3SbS_3 (Fig. 4c and d).

X-ray photoelectron spectroscopy (XPS) analysis confirms the presence of all constituent elements within the nanocrystals, with no detectable impurities observed (Fig. S6). The Cu 2p region exhibits two prominent peaks at binding energies of 932.15 eV and 951.56 eV, corresponding to Cu $2p_{3/2}$ and Cu $2p_{1/2}$, respectively.[46,47] The absence of a satellite peak near 942 eV confirms the exclusive presence of Cu^{1+} oxidation state and excludes the presence of Cu^{2+} species.[47] A doublet at approximately 160.68 eV and 161.69 eV can be attributed to the S $2p_{3/2}$ and S $2p_{1/2}$ levels, respectively.[48] The Sb 3p spectrum displays binding energies at 767.2 eV (Sb $3p_{3/2}$) and 813.46 eV (Sb $3p_{1/2}$), which are consistent with the expected values for Sb^{3+} oxidation state.[49] These results collectively confirm the compositional purity and the oxidation states of the constituent elements in the nanocrystals.

After successful stabilisation of the cubic Cu_3SbS_3 phase at the nanoscale, we have investigated the influence of temperature on its metastability. Fig. 5 shows the heating–cooling differential scanning calorimetry (DSC) measurements data of cubic Cu_3SbS_3 nanocrystals. The DSC data show a strong, well-defined λ-shaped endothermic event with an onset at ~673 K

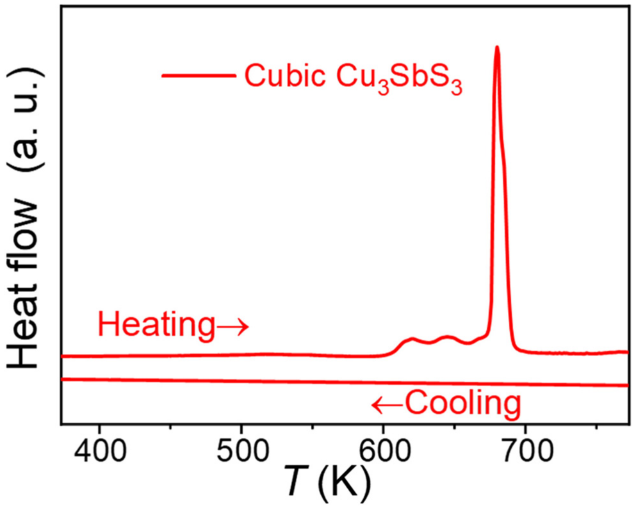

Fig. 5 Temperature-dependent heating–cooling Differential Scanning Calorimetry (DSC) plot of the synthesised Cu_3SbS_3 nanocrystals.

and reaching a peak maximum at ~679 K. This process is attributed to a phase transformation of the metastable cubic Cu_3SbS_3 to the thermodynamically stable phases. The relatively narrow temperature range over which this event occurs suggests a sharp and well-defined transformation. More specifically, the material undergoes a transition to a mixed-phase assemblage comprising two distinct tetrahedrite-type polymorphs and an orthorhombic phase, as further corroborated by high-temperature powder X-ray diffraction (PXRD) analysis, which will be discussed in a later section. Two weak endothermic peaks (~620 and ~645 K) might be associated with the structural relaxation/local phase transformation. This observation indicates the metastable nature of the cubic phase, which exists due to kinetic trapping, and thermal energy supply helps to overcome the thermodynamic barrier for conversion to the stable form. The cooling curve also confirms its irreversible phase transition with the absence any additional peaks.[39]

Temperature-dependent PXRD measurements were performed to probe the structural evolution in metastable cubic Cu_3SbS_3 (Fig. 6). The *in situ* diffraction pattern shows that the cubic phase remains stable up to 623 K, which is consistent with DSC results. Upon further rise of temperature at 648 K, we observed the appearance of additional peaks along with the cubic Cu_3SbS_3 phase (Fig. 6a), indicating the onset of a thermally activated structural change/decomposition in the system. These additional peaks are identified due to the formation of Cu_3SbS_4 phase (space group ($I\bar{4}2m$)) (Fig. 6b and c). The intensity of these additional peaks becomes more prominent at higher temperatures, as evident from the PXRD pattern at ~683 K and 693 K. The transformation was observed to commence around the similar temperature ranges as identified in

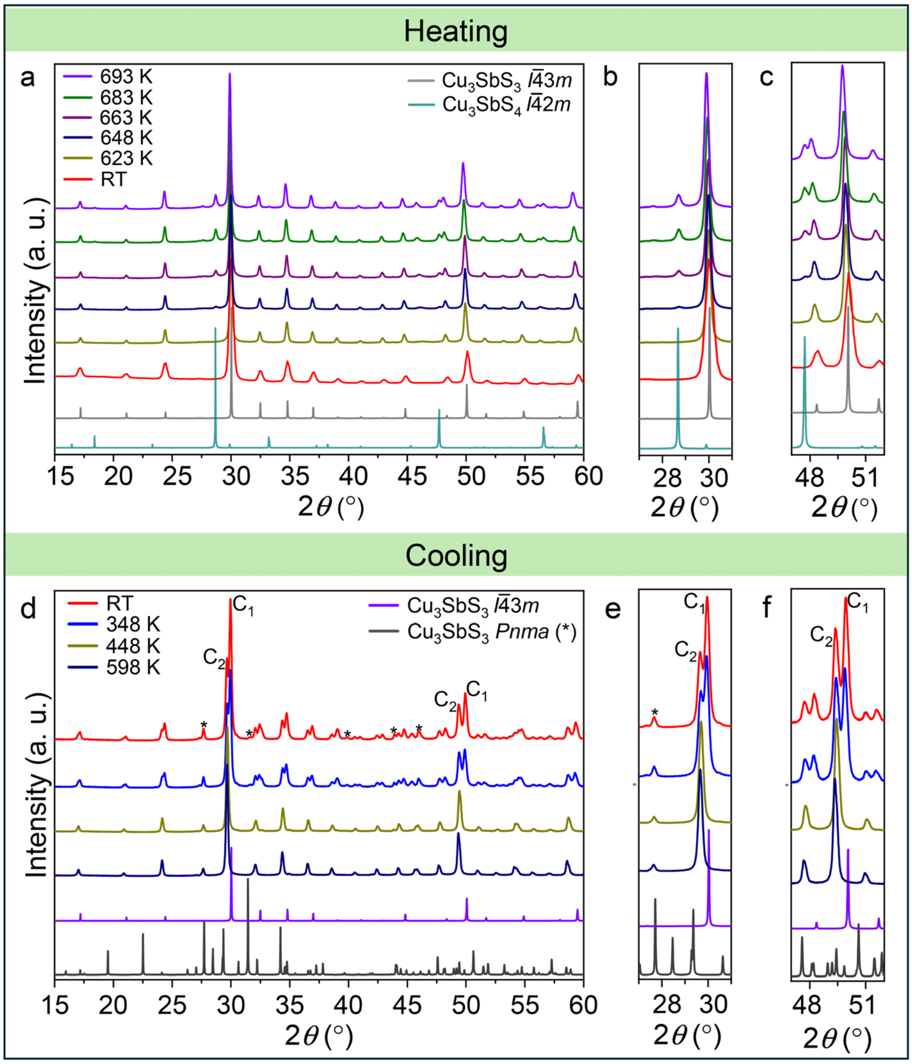

Fig. 6 Temperature-dependent PXRD of nanocrystalline Cu_3SbS_3 showing an irreversible phase transition. (a–c) Heating cycle. (b and c) Magnified views of the PXRD patterns shows the transition to S-rich and S-deficient phases at higher temperature. (d–f) Cooling cycle data, revealing the decomposition of Cu_3SbS_3 into a mixture of tetrahedrite-type cubic phases (C_1 and C_2) and an orthorhombic *Pnma* phase (marked with an asterisk). (e and f) Magnified views of key regions of the PXRD pattern depicting these phases.

DSC measurements. The secondary phase formed at elevated temperatures is structurally consistent with Cu_3SbS_4 and is relatively sulfur-rich compared to cubic Cu_3SbS_3. However, given the complex thermal behavior of metal sulfides, including sulfur volatility and defect formation, the high-temperature phases detected above 648 K may accommodate compositional variation through nonstoichiometry and defect formation rather than representing perfectly stoichiometric compounds.[50] It must be mentioned that the subsequent cooling does not recover the original cubic pattern, confirming the metastable nature of the cubic phase (Fig. 6b). The material decomposed to a mixed-phase assemblage comprising two distinct cubic tetrahedrite-type polymorphs (Fig. 6e and f) marked as C_1 and C_2, and an orthorhombic phase (marked with an asterisk, Fig. 6d), as evident by cooling cycle PXRD analysis. Therefore, the transformation is irreversible in nature and highlights the kinetic stabilisation of cubic Cu_3SbS_3 at nanoscale. The results also confirm that the cubic polymorph cannot revert once transformed, emphasising the importance of kinetically controlled, low-temperature synthetic methods for accessing and stabilising metastable phases that are otherwise inaccessible under equilibrium conditions.

Defect plays an important role in the phase transition/decomposition of solids. To understand the role of defects in the present case, we have performed a positron annihilation spectroscopy (PAS) study. PAS is a powerful technique for detecting vacancies or defect types in solids. The positron annihilation lifetime spectrum (Fig. 7a) of the pristine and 673 K annealed Cu_3SbS_3 sample has been best fitted (using PATFIT 88 computer code) with three lifetime components. Table 1 presents the different lifetime components and their intensities. The source component measured with a pure Al and pure silicon sample has been well taken care during the extraction of lifetime components. It shows a very long lifetime component of 1532 ps to 1715 ps with an intensity of 3%. This is very common in the polycrystalline samples, and the origin of such long component is the pick off annihilation process, *i.e.*, positron initially formed an *ortho*-positronium (spin triplet state) with an electron and subsequently decay with another electron with opposite spin as *para* positronium (spin singlet state). The intermediate lifetime component (τ_2) represents the lifetime of the positrons annihilating in a defect site. The value of the intermediate lifetime component reduces from 348 ps to 316 ps, and the intensity (I_2) decreases from 68% to 65% due to annealing at 673 K (the positron annihilation was done at room temperature). The typical value of positron lifetime in pure sulphur is 300 ps (ref. 51) and the negatively charged sulphur vacancy reduces the position lifetime value. The shortest lifetime component, τ_1 is the free annihilation of positron at the bulk of the sample, which decreases from 188 ps to 144 ps also the average positron lifetime (τ_{ave}) decreases to 259 ps from 300 ps due to annealing. The present experimental result suggests the formation of a sulphur vacancy along with the existing cation defect due to annealing at 673 K.

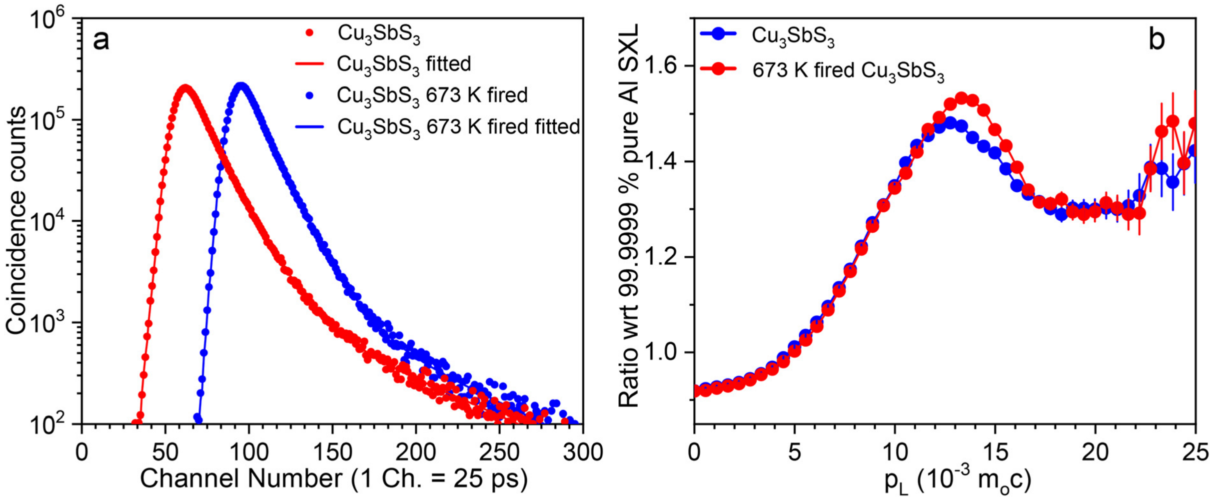

Fig. 7 (a) Positron annihilation lifetime spectra for cubic nanocrystalline Cu_3SbS_3. (b) The area normalised point by point ratio between the CDB spectra of Cu_3SbS_3 and 673 K annealed Cu_3SbS_3 with the CDB spectra of defect-free 99.9999% pure aluminium.

Table 1 Different lifetime components and their intensities

Sample	τ_1 (ps)	I_1 (%)	τ_2 (ps)	I_2 (%)	τ_3 (ps)	I_3 (%)
Cu_3SbS_3 pristine	188 ± 5	29 ± 2	348 ± 6	68 ± 2	1532 ± 32	3 ± 0.2
Cu_3SbS_3 fired at 673 K	144 ± 4	32 ± 2	316 ± 5	65 ± 2	1715 ± 36	3 ± 0.2

The coincidence Doppler broadening (CDB) spectroscopy has been employed to understand the chemical nature of the defect. The CDB data has been analysed by constructing a ratio curve. In the present case, the ratio curve has been constructed between the area-normalised CDB spectra for the 673 K annealed Cu_3SbS_3 sample with the area-normalised CDB spectra of the pristine Cu_3SbS_3 sample (Fig. 7b). The coincidence Doppler broadening spectra of Cu_3SbS_3 and 673 K annealed Cu_3SbS_3 sample has been constructed with the CDB spectra of a defect-free 99.9999% pure Al single crystal (Fig. 7b). In the figure, we find a peak around the momentum value $13 \times 10^{-3} m_o c$. In the positron annihilation process, just before annihilation, positrons are thermalised *i.e.*, their energy is in the order of meV, but the annihilating electrons have some kinetic energy. The kinetic energy of the electron, E_k, can be estimated using the Virial approximation[52] (in the atom, the expectation value of the kinetic energy of an electron, E_{kin}, is equal to the binding energy of the electron), as $E_k = p_L^2/2m_o$. Considering the momentum value of $13 \times 10^{-3} m_o c$, the corresponding kinetic energy of the electron has been calculated as 43 eV. In the present sample, Cu_3SbS_3 the electrons energy of 43 eV is very close to the 4d electron of the Sb (32 eV) atom.[53] The peak height has been increased due to annealing of the Cu_3SbS_3 sample at 673 K, suggest the positrons are more exposed to the 4d electrons of Sb. Since, lifetime data indicate the formation of anion vacancy and ratio curve of CDB spectra shows more annihilation of positrons with 4d electrons of Sb atom, it is therefore concluded that due to annealing of the Cu_3SbS_3 sample sulfur-deficient sites has been generated in the sample. This observation suggests that the formation of Sb and S vacancy defects concentration after heating plays a critical role in the irreversible transformation of cubic Cu_3SbS_3 nanocrystals to orthorhombic Cu_3SbS_3 and non-stoichiometric tetrahedrite phases.

The semiconducting nature of the compound, presence of lone pair electrons on the Sb and open isosceles $[CuS_2\lozenge]$ configuration motivated us to investigate the thermoelectric properties of cubic Cu_3SbS_3 nanocrystals. To measure their thermoelectric properties, we treated the as-synthesised nanocrystals with hydrazine and chloroform to remove any surface-adsorbed ligands. The treated sample was hot-pressed under vacuum in a graphite die by applying a pressure of 50 MPa at 523 K for 30 min. The density of the hot-pressed sample was ~90% of the theoretical density. At 335 K, the σ values for Cu_3SbS_3 sample was ~245 S cm^{-1}, increasing to ~335 S cm^{-1} at 434 K, indicating the semiconducting nature (Fig. 8a). Upon further heating, σ values start to decrease and reaches a value of ~6.3 S cm^{-1} at 725 K. The σ values show variation in trend

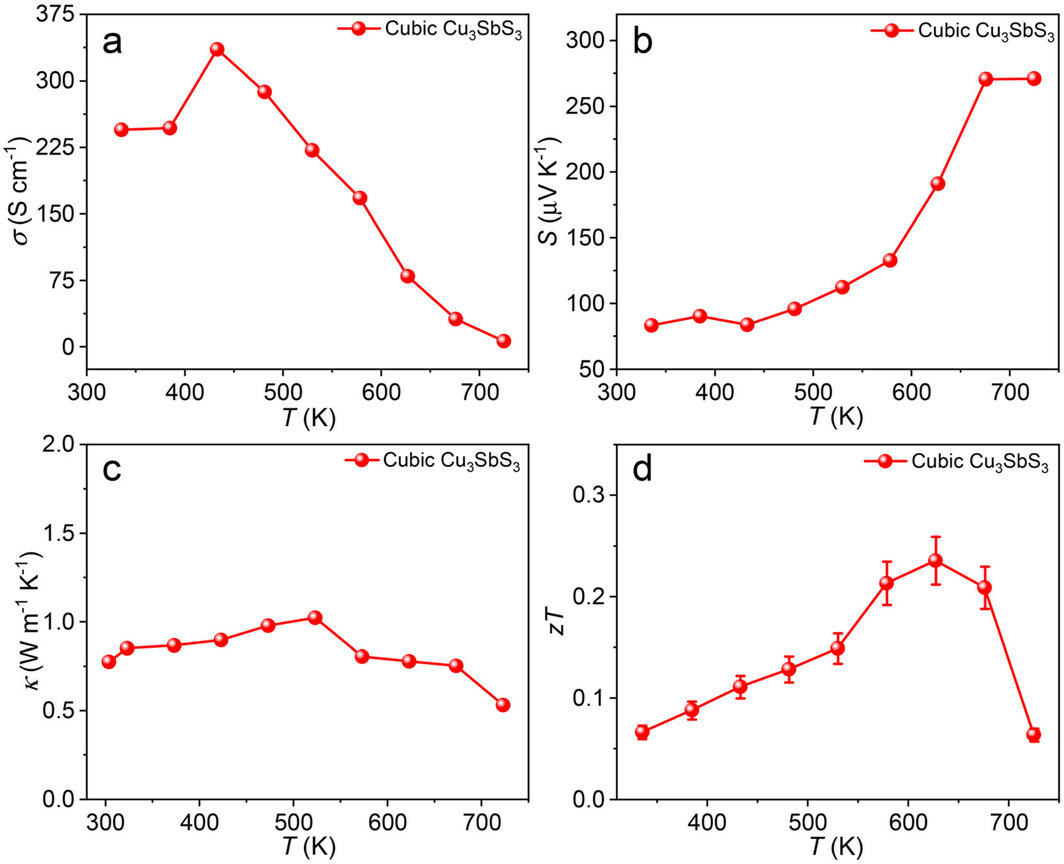

Fig. 8 Temperature-dependent (a) electrical conductivity (σ), (b) Seebeck coefficient (S), (c) thermal conductivity (κ), and (d) thermoelectric figure of merit (zT) of hot-pressed cubic Cu_3SbS_3. A 10% error bar is shown for zT estimation.

above and below ~450 K. Moreover, as discussed previously two weak endothermic peaks (~620 and ~645 K) in DSC could be associated with the structural relaxation/local phase transformation. Overall, structural relaxation/local phase transformation at higher temperature might be the reason for the observed anomaly in electrical conductivity.[39,54] The positive Seebeck coefficient (S) indicates p-type conduction behaviour. At 335 K, the S values for the Cu_3SbS_3 sample was ~83 μV K^{-1} (Fig. 8b) and remains nearly flat up to 481 K (~96 μV K^{-1}), followed by a steep rise at higher temperature and reaches a value of ~271 μV K^{-1} at 725 K. It must be mentioned that subsequent cooling cycle data is not reversible in nature due to metastable nature of the nanocrystal as discussed in previous sections (Fig. S7). Hot pressed Cu_3SbS_3 sample exhibits low thermal-conductivity (κ) ~0.77 W m^{-1} K^{-1} at 303 K, which further decreased to ~0.52 W m^{-1} K^{-1} at 725 K (Fig. 8c). Since the sample has ~90% of the theoretical density, we have also applied a porosity correction to κ values. The porosity correction leads to a slight increase in κ values within the measurement temperature range.[55–57] It shows a value of ~0.89 W m^{-1} K^{-1} at 335 K (Table S3 and Fig. S10). The lattice thermal conductivity (κ_L) was determined by subtracting the electronic contribution (κ_e) from the total thermal conductivity (κ) using the Wiedemann–Franz law relation, $\kappa_e = L\sigma T$, where L is the Lorenz number, and T is the temperature. This analysis reveals that the nanocrystals possess a low lattice thermal conductivity ~0.69 W m^{-1} K^{-1} at 335 K (Fig. S8). The ultralow κ originates from the strong lattice anharmonicity induced by stereochemically active Sb $5s^2$ lone pairs.[44,58] Moreover, in the triangular $[CuS_3]$ coordination environments of cubic Cu_3SbS_3, the absence of one sulfur atom (denoted as ◊) gives rise to an open isosceles $[CuS_2\lozenge]$ configuration, which leads to an increase in the degree of freedom for the atoms. Such an increase in degrees of freedom can leverage additional displacement of the atom from its mean position. An atomic displacement parameter (ADP), a measure of the mean square displacement of an atom from its position, reflects this. Rietveld refinement of the PXRD pattern (Fig. S2) reveals a Cu2 atom in the isosceles $[CuS_2\lozenge]$ configuration at RT, exhibits U_{iso} ~0.01050 $Å^2$ (Table S1), which is ~1.24 times higher than the Cu1 atom from the CuS_4 tetrahedron (U_{iso} ~0.00848 $Å^2$). Such elevated ADPs are characteristic of rattlers,[59,60] whose vibrations strongly scatter the heat-carrying phonons. Thus, anharmonicity induced by the Sb $5s^2$ lone pair and 'rattling'-like Cu vibrations synergistically lead to ultralow thermal conductivity. Finally, we have estimated the thermoelectric figure of merit (zT) of hot pressed cubic Cu_3SbS_3, which shows a peak zT of ~0.23 at 627 K (Fig. 8d).

Conclusion

In summary, we have demonstrated the successful stabilisation of the metastable cubic polymorph of Cu_3SbS_3 at room temperature in nanocrystalline form using a simple low-temperature solution-phase approach. Comprehensive structural and spectroscopic characterisations confirm the formation of phase-pure cubic nanocrystals with a direct band gap of ~1.8 eV, distinct from the bulk monoclinic phase. Thermal analyses, high temperature PXRD and PAS study reveals that the cubic phase remains kinetically stabilised up to ~623 K, beyond which it irreversibly transforms into orthorhombic and tetrahedrite-type structures, assisted by Sb and S vacancy formation. Furthermore, nanocrystals exhibit p-type semiconducting behaviour and a low thermal conductivity of ~0.77 W m^{-1} K^{-1} at 303 K. The ultralow κ originates from strong lattice anharmonicity induced by stereochemically active Sb $5s^2$ lone pairs and local Cu coordination distortions. The results highlight the critical role of nanoscale synthesis and kinetic control in accessing otherwise inaccessible polymorphs, thereby expanding the phase space of functional chalcogenides. The insights gained from this work not only advance the understanding of structural stability and transformation pathways in Cu_3SbS_3 but also provide a framework for the rational design of metastable phases with tailored optoelectronic and thermoelectric properties.

Author contributions

S. N. G. conceived the idea and designed the study. R. D. and A. K. B. M., carried out the synthesis, structural, other characterisation, and analysis of the data. P. N. and S. B. carried out HT-PXRD and thermoelectric measurements, respectively. D. S. carried out the PAS study. All authors contributed to writing and editing the manuscript.

Conflicts of interest

There are no conflicts to declare.

Data availability

The data are available within the article and supplementary information (SI). Supplementary information: experimental details: synthesis, PXRD, FESEM, TEM, XPS, DSC, band gap measurement, PAS, and thermoelectric measurements. Temperature dependent crystal structural evolution in Cu_3SbS_3 (Fig. S1), Rietveld refinement powder pattern of cubic Cu_3SbS_3 (Fig. S2) and structural parameters of the refinement (Table S1), EDX spectra (Fig. S3), TEM and particle size distribution (Fig. S4), comparison plot of PXRD (Fig. S5), XPS (Fig. S6), electrical conductivity and Seebeck coefficient during the heating–cooling cycle (Fig. S7), thermal diffusivity, specific heat capacity, and lattice thermal conductivity (Fig. S8), optical band gap of monoclinic bulk Cu_3SbS_3 (Fig. S9), porosity corrected thermal conductivity and thermoelectric figure of merit (Fig. S10), crystallite size determination (Table S2), thermal conductivity with porosity correction (Table S3) and zT comparison table (Table S4). See DOI: https://doi.org/10.1039/d6nr00071a.

Acknowledgements

This work is supported by the Core Research Grant (CRG) (CRG/2022/004125), Anusandhan National Research Foundation (ANRF), Govt. of India and New Faculty Seed Grant, BITS Pilani. S. N. G. thanks Max Planck Partner Group, Max Planck Society, Germany. R. D. acknowledges CRG for a project fellowship, A. K. B. M. thanks BITS Pilani for a Ph.D. fellowship, and P. N. acknowledges IISER Bhopal for providing a fellowship. S. B. thanks JNCASR for the fellowship. The authors acknowledge the Central Analytical Laboratory of BITS-Pilani, Hyderabad Campus, for providing the facilities. The authors also acknowledge the CIF facilities of IISER Bhopal for temperature-dependent PXRD.

References

1 W. Sun, S. T. Dacek, S. P. Ong, G. Hautier, A. Jain, W. D. Richards, A. C. Gamst, K. A. Persson and G. Ceder, *Sci. Adv.*, 2016, **2**, e1600225.
2 J. L. Fenton and R. E. Schaak, *Angew. Chem., Int. Ed.*, 2017, **56**, 6464–6467.
3 J. Hong, J.-H. Bae, H. Jo, H.-Y. Park, S. Lee, S. J. Hong, H. Chun, M. K. Cho, J. Kim, J. Kim, Y. Son, H. Jin, J.-Y. Suh, S.-C. Kim, H.-K. Roh, K. H. Lee, H.-S. Kim, K. Y. Chung, C. W. Yoon, K. Lee, S. H. Kim, J.-P. Ahn, H. Baik, G. H. Kim, B. Han, S. Jin, T. Hyeon, J. Park, C. Y. Son, Y. Yang, Y.-S. Lee, S. J. Yoo and D. W. Chun, *Nature*, 2022, **603**, 631–636.
4 J. Ravnik, M. Diego, Y. Gerasimenko, Y. Vaskivskyi, I. Vaskivskyi, T. Mertelj, J. Vodeb and D. Mihailovic, *Nat. Commun.*, 2021, **12**, 2323.
5 M. Aykol, S. S. Dwaraknath, W. Sun and K. A. Persson, *Sci. Adv.*, 2017, **3**, eaq0148.
6 M. G. Kanatzidis, *Chem. Mater.*, 1990, **2**, 353–363.
7 D. P. Shoemaker, Y.-J. Hu, D. Y. Chung, G. J. Halder, P. J. Chupas, L. Soderholm, J. F. Mitchell and M. G. Kanatzidis, *Proc. Natl. Acad. Sci. U. S. A.*, 2014, **111**, 10922–10927.
8 M. G. Kanatzidis, R. Pöttgen and W. Jeitschko, *Angew. Chem., Int. Ed.*, 2005, **44**, 6996–7023.
9 A. Parija, G. R. Waetzig, J. L. Andrews and S. Banerjee, *J. Phys. Chem. C*, 2018, **122**, 25709–25728.
10 B. J. Beberwyck, Y. Surendranath and A. P. Alivisatos, *J. Phys. Chem. C*, 2013, **117**, 19759–19770.
11 L. De Trizio and L. Manna, *Chem. Rev.*, 2016, **116**, 10852–10887.
12 D. H. Son, S. M. Hughes, Y. Yin and A. P. Alivisatos, *Science*, 2004, **306**, 1009–1012.
13 X. Zhang, N. Tran, T. Egan, B. Sharma and G. Chen, *J. Phys. Chem. C*, 2021, **125**, 13350–13360.
14 N. Soltani, E. Saion, M. Z. Hussein, R. Yunus and M. Navaseri, *Adv. Mater. Res.*, 2013, **667**, 122–127.
15 C. Li, Y. Wei, A. Liivat, Y. Zhu and J. Zhu, *Mater. Lett.*, 2013, **107**, 23–26.
16 J. V. I. Timonen, E. T. Seppälä, O. Ikkala and R. H. A. Ras, *Angew. Chem., Int. Ed.*, 2011, **50**, 2080–2084.
17 S. N. Guin, S. Banerjee, D. Sanyal, S. K. Pati and K. Biswas, *Chem. Mater.*, 2017, **29**, 3769–3777.
18 S. He, L. Zhu, J. Zhou and Z. Sun, *Inorg. Chem.*, 2017, **56**, 11990–11997.
19 R. B. Soriano, I. U. Arachchige, C. D. Malliakas, J. Wu and M. G. Kanatzidis, *J. Am. Chem. Soc.*, 2013, **135**, 768–774.
20 M. E. Norako and R. L. Brutchey, *Chem. Mater.*, 2010, **22**, 1613–1615.
21 M. E. Norako, M. J. Greaney and R. L. Brutchey, *J. Am. Chem. Soc.*, 2012, **134**, 23–26.
22 A. Singh, H. Geaney, F. Laffir and K. M. Ryan, *J. Am. Chem. Soc.*, 2012, **134**, 2910–2913.
23 X. Lu, Z. Zhuang, Q. Peng and Y. Li, *Chem. Commun.*, 2011, **47**, 3141.
24 B. A. Tappan, B. Zhu, P. Cottingham, M. Mecklenburg, D. O. Scanlon and R. L. Brutchey, *Nano Lett.*, 2021, **21**, 5881–5887.
25 K. Senevirathne, R. Tackett, P. R. Kharel, G. Lawes, K. Somaskandan and S. L. Brock, *ACS Nano*, 2009, **3**, 1129–1138.
26 R. B. Soriano, C. D. Malliakas, J. Wu and M. G. Kanatzidis, *J. Am. Chem. Soc.*, 2012, **134**, 3228–3233.
27 I. T. Sines, R. Misra, P. Schiffer and R. E. Schaak, *Angew. Chem., Int. Ed.*, 2010, **49**, 4638–4640.
28 Z. Sun, Y. Chen and R. L. Brutchey, *J. Am. Chem. Soc.*, 2025, **147**, 21219–21230.
29 A. Ashok, A. Vasanth, T. Nagaura, C. Setter, J. K. Clegg, A. Fink, M. K. Masud, M. S. Hossain, T. Hamada, M. Eguchi, H. P. Phan and Y. Yamauchi, *J. Am. Chem. Soc.*, 2023, **145**, 23461–23469.
30 K. Chen, B. Du, N. Bonini, C. Weber, H. Yan and M. J. Reece, *J. Phys. Chem. C*, 2016, **120**, 27135–27140.
31 B. Du, R. Zhang, K. Chen, A. Mahajan and M. J. Reece, *J. Mater. Chem. A*, 2017, **5**, 3249–3259.
32 R. Zhang, K. Chen, B. Du and M. J. Reece, *J. Mater. Chem. A*, 2017, **5**, 5013–5019.
33 B. Du, K. Chen, H. Yan and M. J. Reece, *Scr. Mater.*, 2016, **111**, 49–53.
34 X. Lu and D. T. Morelli, *Phys. Chem. Chem. Phys.*, 2013, **15**, 5762.
35 X. Lu, D. T. Morelli, Y. Xia, F. Zhou, V. Ozolins, H. Chi, X. Zhou and C. Uher, *Adv. Energy Mater.*, 2013, **3**, 342–348.
36 E. J. Skoug and D. T. Morelli, *Phys. Rev. Lett.*, 2011, **107**, 235901.
37 Y. Huang, B. Zhang, J. Li, Z. Zhou, S. Zheng, N. Li, G. Wang, D. Zhang, G. Han, X. Han, X. Lu and X. Zhou, *Adv. Mater.*, 2022, **34**, 2109952.
38 D. Zhang, X. Wang, H. Wu, Y. Huang, S. Zheng, B. Zhang, H. Fu, Z. Cheng, P. Jiang, G. Han, G. Wang, X. Zhou and X. Lu, *Adv. Funct. Mater.*, 2023, **33**, 2214163.
39 B. Du, R. Zhang, M. Liu, K. Chen, H. Zhang and M. J. Reece, *J. Mater. Chem. C*, 2019, **7**, 394–404.
40 A. Pfitzner, *Zeitschrift für Kristallographie*, 1998, **213**, 228–236.

41 H. J. Whitfield, *Solid State Commun.*, 1980, **33**, 747–748.

42 K. Chen, PhD thesis, Queen Mary University of London, London, UK, 2016.

43 K. Tatsuka and N. Morimoto, *Econ. Geol.*, 1977, **72**, 258–270.

44 L. Li, J. Wan, C. Lin, Y. Wu, Z. Cheng, Y. Lin, S. Yang and M. Luo, *Small*, 2025, **21**, e202503137.

45 R. Santhanapriya, A. Muthukannan, G. Sivakumar and K. Mohanraj, *Synth. React. Inorg., Met.-Org., Nano-Met. Chem.*, 2016, **46**, 1388–1394.

46 H. Liu, Z. Yu, L. Liu and S. Dong, *ACS Appl. Mater. Interfaces*, 2024, **16**, 33038–33052.

47 M. X. Wang, G. H. Yue, X. Y. Fan and P. X. Yan, *J. Cryst. Growth*, 2008, **310**, 3062–3066.

48 J. E. Daniel, S. I. Weaver, B. R. Matthias, R. Golden, G. M. George, C. Kerpal, C. L. Donley, L. E. Jarocha and M. E. Anderson, *J. Phys. Chem. C*, 2024, **128**, 13888–13899.

49 Y. Ma, C. Ma, H. Yi, H. Liang, W. Wang, Z. Zheng, Y. Zou, Z. Deng, J. Yao and G. Yang, *Adv. Opt. Mater.*, 2023, **11**, 2302039.

50 G. Li, B. Zhang, F. Yu, A. A. Novakova, M. S. Krivenkov, T. Y. Kiseleva, L. Chang, J. Rao, A. O. Polyakov, G. R. Blake, R. A. de Groot and T. T. M. Palstra, *Chem. Mater.*, 2014, **26**, 5821–5829.

51 R. Domínguez-Reyes and A. Rodríguez-López, *Mater. Res. Express*, 2022, **9**, 026521.

52 U. Myler and P. J. Simpson, *Phys. Rev. B: Condens. Matter Mater. Phys.*, 1997, **56**, 14303–14309.

53 https://www.webelements.com.

54 J. Wang, T. Wang, J. Zhang, B. Liu, L. Wang, W. Gu, B. Hu, J. Xu and B. Du, *J. Solid State Chem.*, 2022, **310**, 123014.

55 L. Zhai, H. Liu, L. Su, Y. Kuang, F. Chen, Y. Zhang, W. Fan and Z. Sun, *Energy Environ. Mater.*, 2025, **8**, e70066.

56 D. Ma, Y. Ma, J. Ma, Q. Yang, C. Felser and G. Li, *Innovation*, 2024, **5**, 100709.

57 D. A. Ferluccio, J. E. Halpin, K. L. MacIntosh, R. J. Quinn, E. Don, R. I. Smith, D. A. MacLaren and J.-W. G. Bos, *J. Mater. Chem. C*, 2019, **7**, 6539–6547.

58 E. J. Skoug and D. T. Morelli, *Phys. Rev. Lett.*, 2011, **107**, 235901.

59 X. Shi, J. Yang, J. R. Salvador, M. Chi, J. Y. Cho, H. Wang, S. Bai, J. Yang, W. Zhang and L. Chen, *J. Am. Chem. Soc.*, 2011, **133**, 7837–7846.

60 M. K. Jana, K. Pal, A. Warankar, P. Mandal, U. V. Waghmare and K. Biswas, *J. Am. Chem. Soc.*, 2017, **139**, 4350–4353.